Available online at www.sciencedirect.com
ScienceDirect
Trans. Nonferrous Met. Soc. China 31(2021) 3012−3023
Transactions of Nonferrous Metals Society of China
www.tnmsc.cn

Microstructures and mechanical properties of Ti−Al−V−Nb alloys with cluster formula manufactured by laser additive manufacturing

Tian-yu LIU[1,2], Xiao-hua MIN[1], Shuang ZHANG[3], Cun-shan WANG[2], Chuang DONG[2,3]

1. School of Materials Science and Engineering, Dalian University of Technology, Dalian 116024, China;
2. Key Laboratory for Materials Modification by Laser, Ion, and Electron Beams (Dalian University of Technology), Ministry of Education, Dalian 116024, China;
3. School of Materials Science and Engineering, Dalian Jiaotong University, Dalian 116028, China

Received 23 December 2020; accepted 28 June 2021

Abstract: Ti−Al−V−Nb alloys with the cluster formula, $12[Al-Ti_{12}](AlTi_2)+5[Al-Ti_{14}](V,Nb)_2Ti$, were designed by replacing V with Nb based on the Ti−6Al−4V alloy. Single-track cladding layers and bulk samples of the alloys with Nb contents ranging from 0 to 6.96 wt.% were prepared by laser additive manufacturing to examine their formability, microstructure, and mechanical properties. For single-track cladding layers, the addition of Nb increased the surface roughness slightly and decreased the molten pool height to improve its spreadability. The alloy, Ti−5.96Al−1.94V−3.54Nb (wt.%), exhibited better geometrical accuracy than the other alloys because its molten pool height was consistent with the spread layer thickness of the powder. The microstructures of the bulk samples contained similar columnar β-phase grains, regardless of Nb content. These grains grew epitaxially from the Ti substrate along the deposition direction, with basket-weave α-phase laths within the columnar grains. The α-phase size increased with increasing Nb contents, but its uniformity decreased. Along the deposition direction, the Vickers hardness increased from the substrate to the surface. The Ti−5.96Al−1.94V−3.54Nb alloy exhibited the highest Vickers hardness regardless of deposition position because of the optimal matching relationship between the α-phase size and its content among the designed alloys.

Key words: Ti−Al−V−Nb alloy; composition design; laser additive manufacturing; microstructure; mechanical properties

1 Introduction

Laser additive manufacturing (LAM) is a near-net shape additive manufacturing method, where a three-dimensional part with complex geometric features can be fabricated layer-by-layer [1,2]. Ti−6Al−4V alloy is used widely in advanced aerospace applications owing to its high specific strength, low density, and excellent corrosion resistance [3]. On the other hand, complex Ti−6Al−4V alloy parts fabricated via traditional wrought processes are expensive, and the process is time-consuming. Hence, the Ti−6Al− 4V components manufactured by LAM have attracted increasing attention in recent years [4,5]. Many studies [6,7] have found that the as-deposited alloy contains columnar prior-β grains that grow epitaxially from the substrate. Compared to wrought components, the Ti−6Al−4V alloys prepared via LAM have higher strength and lower ductility. Rapid cooling of as-deposited samples of Ti−6Al−4V alloys manufactured using LAM forms an ultrafine α phase and α' martensite, resulting in high strength and low ductility [8,9]. The study by VILARO et al [10] and LI et al [11] suggested that

Corresponding author: Xiao-hua MIN, Tel/Fax: +86-411-84708389, E-mail: minxiaohua@dlut.edu.cn;
Chuang DONG, Tel/Fax: +86-411-84708389, E-mail: dong@dlut.edu.cn
DOI: 10.1016/S1003-6326(21)65711-4

the occurrence of pores could be the precursor of adiabatic shear bands and micro-cracks, thus reducing the ductility.

Heat treatment has been confirmed to be one of the most effective ways to improve the ductility of an alloy. VRANCKEN et al [12] reported a 7% to 13% improvement in ductility when the Ti−6Al−4V alloys manufactured by LAM are annealed at 850 °C for 2 h, followed by furnace cooling. REN et al [13] suggested that Ti−6Al−4V alloys prepared via LAM and then subjected to a solution treatment at 920 °C for 2 h followed by aging at 550 °C for 4 h showed a ductility of up to 18%. ZHAO et al [14] reported that the ductility was significantly enhanced to 25% when Ti−6Al−4V alloys manufactured via LAM were annealed sub-critically at 980 °C for 1 h, solution-treated at 920 °C for 1 h, and aged at 550 °C for 4 h. SABBAN et al [15] reported that after heating to 975 °C at 5 °C/min, followed by thermal cycling between 975 °C and 875 °C, the ductility of the Ti−6Al−4V alloys prepared via LAM was improved to 18%, whereas post-heat treatments could lead to a distortion of the sample and the sacrifice of strength.

The microstructure and mechanical properties of the Ti−6Al−4V alloys manufactured via LAM can be optimized by alloying. SUI et al [16] examined the effects of Nb addition on the mechanical properties and corrosion behavior of a mixture of Ti−6Al−4V and powder with 5 at.% Nb by selective laser melting. The resulting alloy exhibited a combination of superior plastic deformation (ε_p=18.9) and high compressive strength (σ_c=1593 MPa). Nb is used widely in Ti alloys because of its low toxicity [17,18].

After a long effort, we have proposed the cluster-plus-glue-atom model to describe short-range-ordered structures [19−21]. Generally, the typical characteristic of solid solutions is chemical short-range order (SRO) of the solute distribution, which can be expressed by covering only the nearest-neighbor cluster and a few glue atoms located at the next outer shell, which are written as a universal molecule-like cluster formula: [cluster](glue atoms)$_x$, where x means the number of glue atoms. The cluster formula approach is effective and efficient in alloy development [22−25].

A previous study revealed the chemical structural origin of Ti−6Al−4V alloys. This alloy is composed of two solid solution phases: an α phase with hexagonal close-packed crystal structure and a β phase with body-centered cubic structure. Firstly, the cluster formulas of the α and β phases were established using measured chemical compositions, such as α-[Al−Ti$_{12}$](AlTi$_2$) and β-[Al−Ti$_{14}$](V$_2$Ti). Then, the relative proportions of α and β phases were determined (i.e., approximately 2.4:1). Finally, a hard-sphere cluster-resonance model was developed, mimicking the atomic-level resonance model of solid solution alloys, where the two structural units were treated as hard spheres with different radii. The calculation gave a unit of 17 hard spheres, which led to the cluster composition formula, 12[Al−Ti$_{12}$](AlTi$_2$)+5[Al−Ti$_{14}$](V$_2$Ti) for Ti−6.05Al−3.94V in wt.%. Therefore, Ti−6Al−4V was chosen as the basic alloy to design the alloy by replacing some of the V with Nb.

This study examined the effects of replacing V with Nb on the microstructure, formability, and mechanical properties based on the Ti−6Al−4V cluster composition formula. The alloy series was 12[Al−Ti$_{12}$](AlTi$_2$)+5[Al−Ti$_{14}$](V,Nb)$_2$Ti according to the aforementioned cluster composition formula. The surface roughness and molten pool size of the single-track laser cladding layer in Ti−Al−V−Nb alloys were investigated to explore the formability. The effects of replacing V with Nb on the microstructure and Vickers hardness of these designed alloys were also investigated.

2 Experimental

2.1 Composition design

Cluster formulism is a new approach to describe short-range-ordered structures because conventional crystallography cannot deal with local disorders. In this study, five multicomponent Ti−Al−V−Nb alloys were designed by replacing V with Nb based on the cluster formula 12[Al−Ti$_{12}$](AlTi$_2$)+5[Al−Ti$_{14}$](V$_2$Ti) of Ti−6Al−4V.

The first step was to determine the position of Nb in the dual-cluster formula. Nb should exist in the β phase cluster formula [Al−Ti$_{14}$](V$_2$Ti) because Nb and V are isomorphous β stable elements. According to the positive mixing enthalpy between Ti and Nb (ΔH_{Ti-Nb}=2 kJ/mol), Nb showed weak interactions with Ti and was considered to occupy the positions of glue atoms with Ti together. Thus,

the cluster composition formula of the alloy was defined as $12[Al-Ti_{12}](AlTi_2)+5[Al-Ti_{14}](V,Nb)_2Ti$. The next step was to determine the Nb content. The cluster-plus-glue-atom model provided chemical composition information and the local atomic configuration, similar to the molecular formulas in chemical substances. Therefore, the number of atoms in the cluster formula must be an integer. Accordingly, the cluster formulas of the five alloys were obtained by replacing V with Nb: $12[Al-Ti_{12}](AlTi_2)+5[Al-Ti_{14}](V_2Ti)$, $12[Al-Ti_{12}](AlTi_2)+5[Al-Ti_{14}](V_{1.4}Nb_{0.6}Ti)$, $12[Al-Ti_{12}](AlTi_2)+5[Al-Ti_{14}]$(VNbTi), $12[Al-Ti_{12}](AlTi_2)+5[Al-Ti_{14}]$ $(V_{0.6}Nb_{1.4}Ti)$, and $12[Al-Ti_{12}](AlTi_2)+5[Al-Ti_{14}]$ (Nb_2Ti). Table 1 lists all compositions of this designed series, with 0Nb and 7Nb corresponding to the industrial Ti−6Al−4V and Ti−6Al−7Nb alloys, respectively.

2.2 Laser additive manufacturing

Ti powder particles with sizes of 50−150 μm, Al powder particles with sizes of 50−75 μm, and V and Nb powder particles with sizes of 50−75 μm were used to prepare the Ti−6Al−4V alloy. Figure 1 presents the scanning electron microscopy (SEM) image of those particles, where the larger and spherical particles are Ti; the smaller and spherical particles are Al; the irregularly shaped particles are V. In the LAM experiments, we used a continuous-wave CO_2 laser system with a power of 5 kW, a building platform, and a computer system. The LAM processing parameters of the single-track cladding layer samples were set as follows: laser power, 1800 W; beam diameter, 3 mm; scanning speed, 9 mm/s; laser scan length of the single-trace cladding layer, 10 mm. The bulk samples were formed by spreading thin layers of powder and fusing this powder pass-by-pass and layers-upon-layer. The processing parameters were as follows: laser power, 1800 W; beam diameter, 3 mm; scanning speed, 9 mm/s; overlap, 30%; thickness of the spread layer of powder, 0.5 mm. Five layers of powder were spread. Figure 2(a) presents a schematic diagram of the LAM processing method. A zigzag scanning strategy for bulk samples was used and rotated by 90° between each layer, as shown in Fig. 2(b).

2.3 Measurement of formability of single-track cladding layers

The formability was characterized by the surface roughness and melt pool size of a single-track cladding layer, whereas the surface roughness was measured using an Olympus confocal laser microscope. The surface roughness was determined by mathematically averaging the measurement results of three single-track cladding layers in each composition. The melt pool size was obtained using an Olympus optical microscope, and three different cross-section positions of each single-track cladding layer were then analyzed by using Image-Pro software.

2.4 Measurement of microstructure and mechanical properties of bulk samples

The deposited bulk samples were divided into two batches. The first was a cross-section near the surface, and the second was a longitudinal section along the deposition direction from the bottom to the top position in the following order: Layer 1 (near the substrate), Layer 2, Layer 3, Layer 4, and Layer 5 (near the surface). The observation position of the microstructure was the longitudinal section along the deposition direction. An etchant containing 90 mL distilled water, 7 mL HNO_3, and 3 mL HF was used to reveal the microstructure. The microstructures of the β grains from Layers 1 to 5 were examined using an Olympus optical microscope. The α grains in Layers 1 and 5 were observed using a Zeiss Supra55 scanning electron microscope. The phase identification was conducted by X-ray diffraction (XRD) at 2θ values of 20°−

Table 1 Designed compositions of Ti−Al−V−Nb alloys based on cluster formulas

Alloy	Cluster formula (at.%)	Composition (wt.%)
0Nb (Ti−6Al−4V)	$12[Al-Ti_{12}](AlTi_2)+5[Al-Ti_{14}](V_2Ti)$	Ti−6.05Al−3.94V
2Nb (Ti−6Al−3V−2Nb)	$12[Al-Ti_{12}](AlTi_2)+5[Al-Ti_{14}](V_{1.4}Nb_{0.6}Ti)$	Ti−5.99Al−2.73V−2.14Nb
3.5Nb (Ti−6Al−2V−3.5Nb)	$12[Al-Ti_{12}](AlTi_2)+5[Al-Ti_{14}]$(VNbTi)	Ti−5.96Al−1.94V−3.54Nb
5Nb (Ti−6Al−1V−5Nb)	$12[Al-Ti_{12}](AlTi_2)+5[Al-Ti_{14}](V_{0.6}Nb_{1.4}Ti)$	Ti−5.92Al−1.16V−4.92Nb
7Nb (Ti−6Al−7Nb)	$12[Al-Ti_{12}](AlTi_2)+5[Al-Ti_{14}](Nb_2Ti)$	Ti−5.86Al−6.96Nb

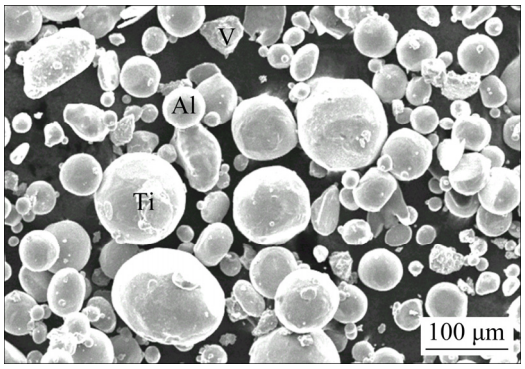

Fig. 1 SEM image of Ti, Al, and V powder mixture for Ti−6Al−4V alloy, with larger spherical particles representing Ti, smaller spherical particles indicating Al, and irregularly shaped particles being V

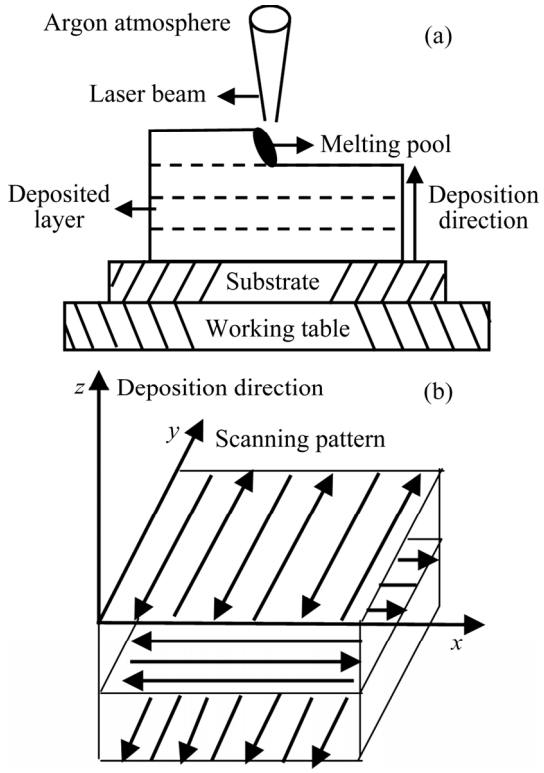

Fig. 2 Schematic diagram of LAM processing method (a) and scanning strategy (b) for bulk samples

100°, with a scanning rate of 4 (°)/min. The X-ray measurements were performed on the cross-section near the surface. The Vickers hardness of the cross and longitudinal sections was obtained using an HVS−1000 apparatus with a load of 500 g for 15 s. Samples of the cross-section near the surface were tested at least 10 times. The Vickers hardness of the longitudinal section along the deposition direction was also measured at least three times at each position.

3 Results and discussion

3.1 Formability of single-track cladding layers

Figure 3 shows the macromorphologies on the surface of single-track cladding layers in Ti−Al−V−Nb alloys. The lightness of the sample surface darkened gradually with increasing Nb content. This was attributed to the unmelted powder on the sample surface. During a low heat input, the delivered energy was insufficient to melt the powder particles completely. The solid powder particles stuck on the surfaces of the build [26−28]. The surface roughness could quantitatively characterize the surface quality of the single-track

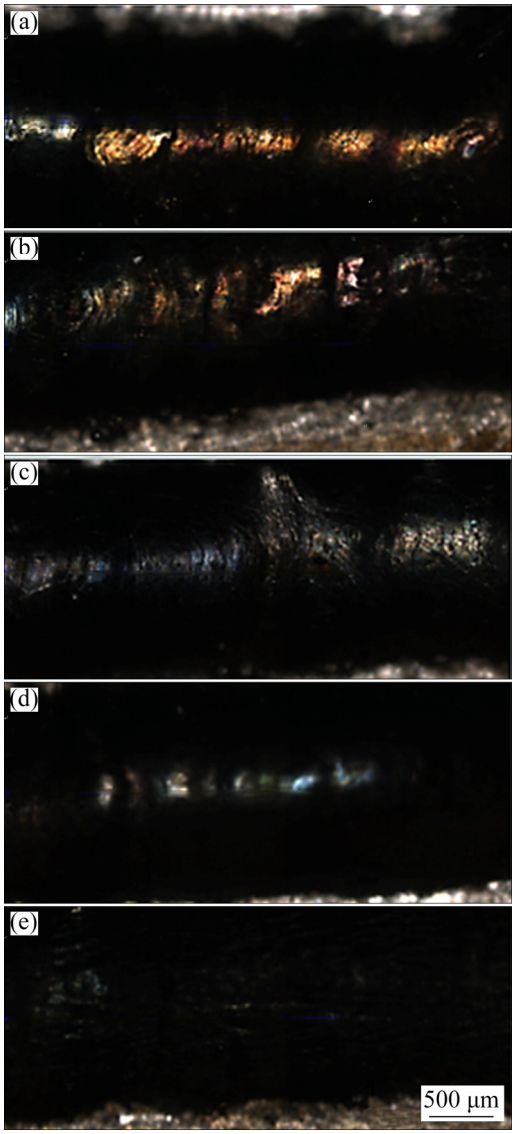

Fig. 3 Macromorphologies on surface of single-track cladding layers in Ti−Al−V−Nb alloys: (a) 0 Nb; (b) 2Nb; (c) 3.5Nb; (d) 5Nb; (e) 7Nb

cladding layers. On the surface, the height of a peak or the depth of a valley was measured on several locations (denoted by N) along the profile length L. Figure 4 presents the changes in the surface roughness of single-track cladding layers in Ti−Al−V−Nb alloys. Some degree of fluctuation appeared in the surface roughness distribution of each sample, and the fluctuation increased slightly with increasing Nb concentration (Figs. 4(a−e)). As shown in Fig. 4(f), with the increase of Nb content, the average surface roughness (R_a) increased from 9.32 to 12.43 μm, suggesting that the addition of Nb reduces the surface quality of the single-track cladding layer slightly.

Figure 5 shows the molten pool morphologies on the cross-section of single-track cladding layers

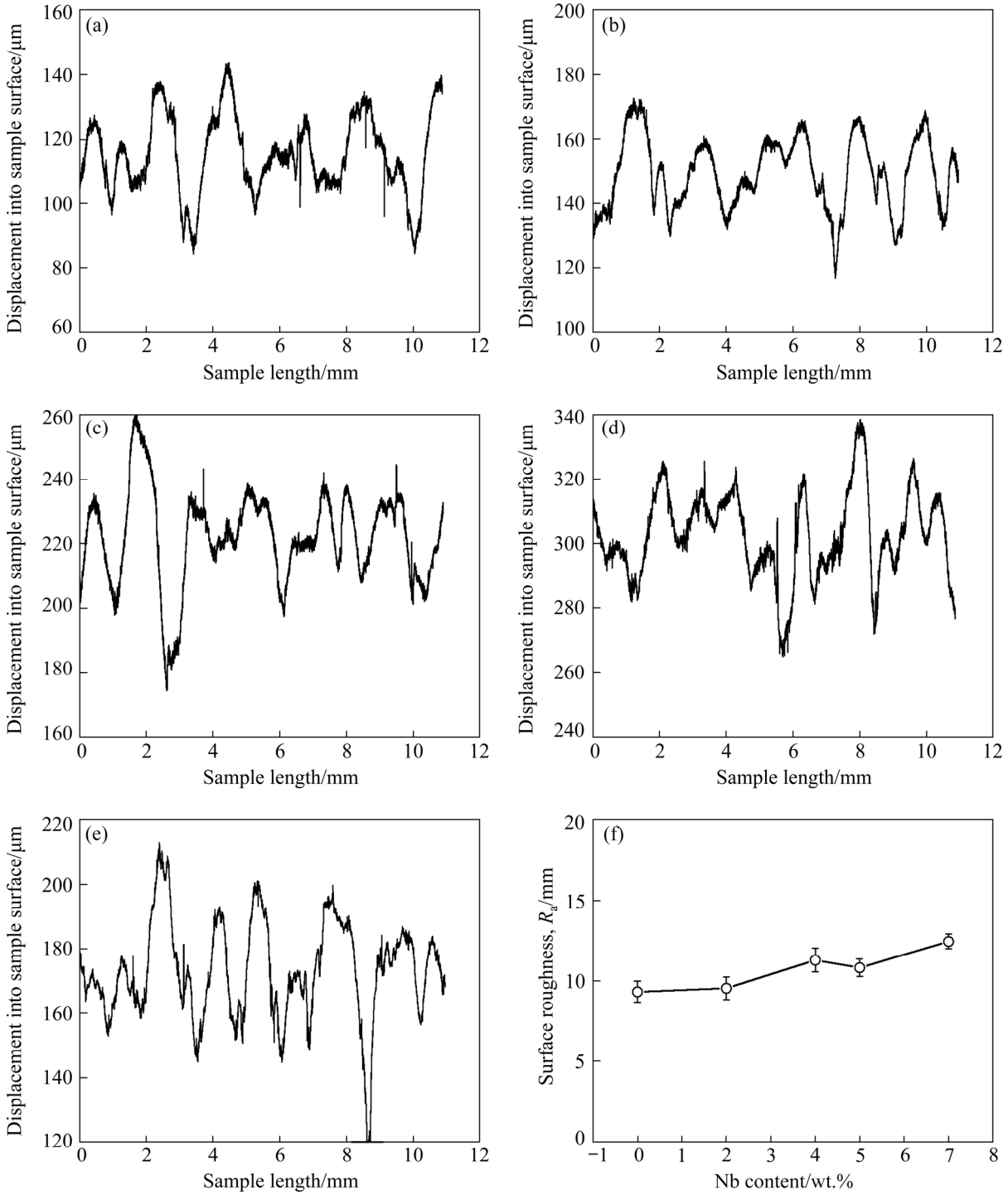

Fig. 4 Height of peak or depth of valley of single-track cladding layers on surface in Ti−Al−V−Nb alloys: (a) 0Nb; (b) 2Nb; (c) 3.5Nb; (d) 5Nb; (e) 7Nb; (f) Changes in surface roughness as function of Nb content

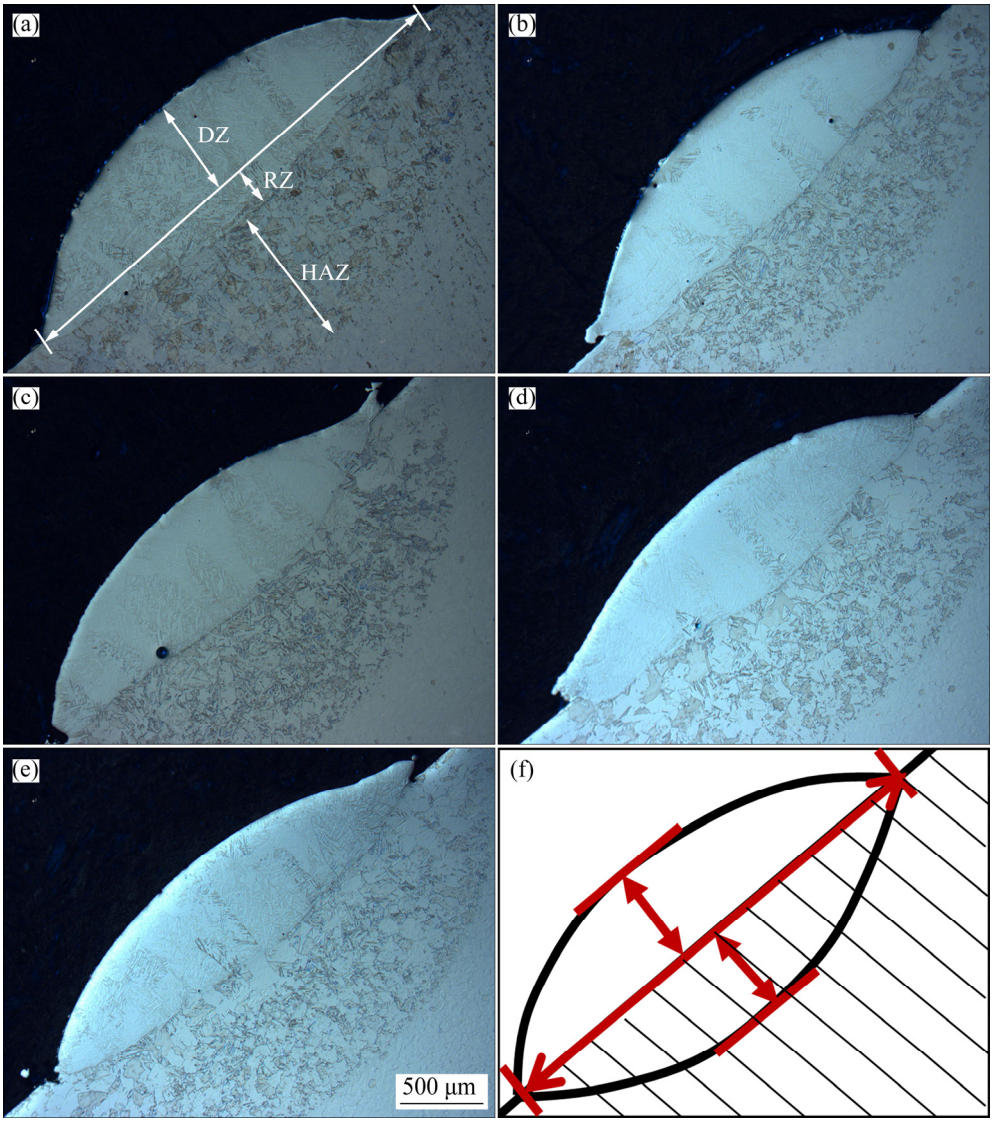

Fig. 5 Molten pool morphologies on cross-section of single-track cladding layers in Ti−Al−V−Nb alloys: (a) 0Nb; (b) 2Nb; (c) 3.5Nb; (d) 5Nb; (e) 7Nb; (f) Schematic diagram of molten pool

in the Ti−Al−V−Nb alloys. The deposition of a single-track on the substrate results in the inevitable remelting of a substrate portion. Hence, the molten pool is composed of the deposition zone (DZ), the remelting zone (RZ), and the heat-affected zone (HAZ), as shown in Fig. 5(a). The depth of the HAZ was relatively constant as the Nb content was increased, i.e., ~800 μm, which was 1.6 times the thickness of the deposited layer. Furthermore, for the molten pool, its height was closely associated with the actual layer thickness, and the width and depth determined the metallurgical bonding capacity directly [29]. Figure 6(a) shows the measured depth (D, mm), width (W, mm), and height (H, mm) of molten pools (Fig. 5(f)). A decrease in height from 600 to 440 μm was observed as the Nb content was increased from 0 to 7 wt.%. The geometrical accuracy was higher when the height of the molten pool was consistent with the thickness of the spread layer of the powder (500 μm). Therefore, when the Nb content was increased from 2 to 3.5 wt.%, the height of the molten pool decreased from 513 to 488 μm, which can improve the geometrical accuracy. Moreover, the width of the molten pools remained constant (2500 μm) when the Nb content increased from 0 to 5 wt.%. In particular, the width of the 7Nb alloy increased to 2600 μm. However, the depth of molten pools remained relatively constant (200 μm) with increasing Nb content, indicating that the metallurgical bonding capacity is similar. Figure 6(b) shows the depth-to-width ratio and

height-to-width ratio of the molten pool. With increasing Nb content from 0 to 7 wt.%, the depth-to-width ratio slightly decreased from 0.9 to 0.8, suggesting that the morphology of the molten pool was under conduction mode (U-shape). In contrast, the height-to-width ratio decreased from 0.24 to 0.17, which is related to the increase in spreadability caused by the addition of Nb.

3.2 Microstructure of bulk samples

Figure 7 shows optical microscopy images on the longitudinal section of the bulk samples in Ti−Al−V−Nb alloys. Columnar β grains were observed regardless of the Nb content. They grew epitaxially from the substrate with deposition. The formation of columnar β grains had two causes. Heat loss initially resulted in more rapid cooling through the substrate, leading to the directional growth of the grains. On the other hand, the narrow solidification range (T_L-T_S, where T_L is the liquidus temperature, and T_S is the solidus temperature) is conducive to the formation of columnar grains, which was calculated using JMatPro software, as shown in Fig. 8(a). The solidification range was 12−17 °C. Generally, the large range causes the solute partition coefficient (k) to be further away from the ideal value of 1, favoring the formation of column grains [30]. Furthermore, the width of the columnar β grains remained constant at approximately 170 μm (Fig. 8(b)), suggesting that Nb had a minimal effect on columnar grains. Gas atomization usually produces pores because the gases trapped during rapid solidification process are transferred to various parts, resulting in powder-induced pores. These pores are spherical, as shown in Figs. 7(a−e). Pores are also formed when the applied energy is insufficient for complete melting. These pores are typically non-spherical, as shown Fig. 7(b). The basket-weave microstructure in the β grains is composed of α laths, as shown in Figs. 7(a−e). Some layer bands and grain boundary α layer (GBα) can also be observed, as indicated by the black arrows in Fig. 7(e). When the powder is deposited on the pre-existing layer, the region that remains solid at the top of the pre-existing layer is reheated. Grain growth can occur in this region,

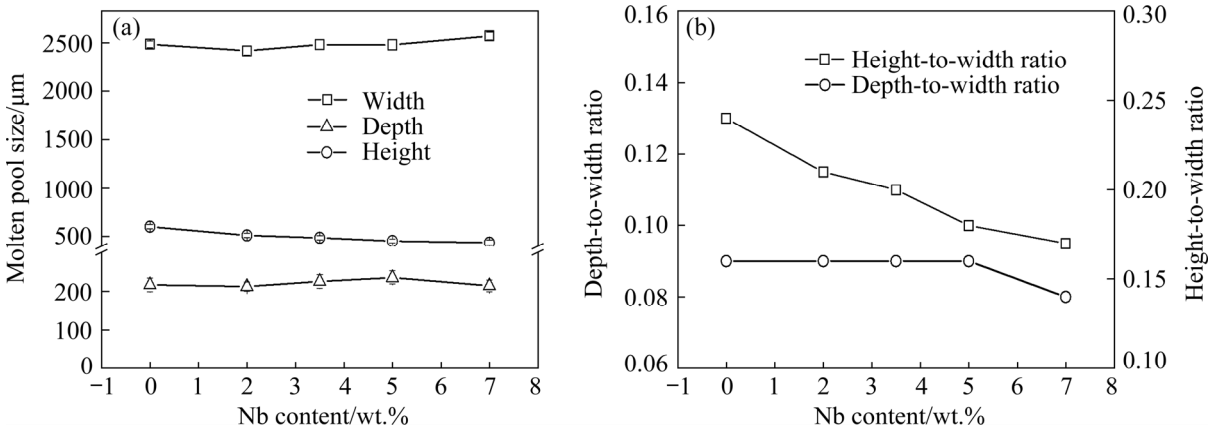

Fig. 6 Changes in molten pool size of single-track cladding layers with Nb content in Ti−Al−V−Nb alloys: (a) Measured depth, width, and height; (b) Depth-to-width ratio and height-to-width ratio

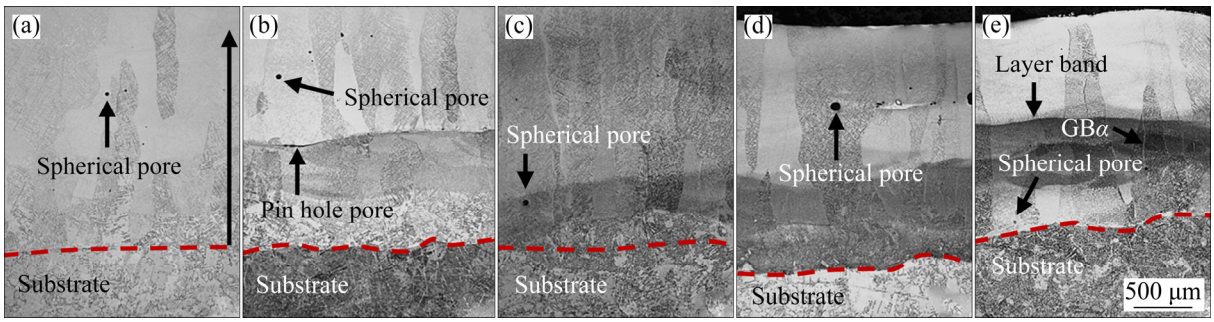

Fig. 7 Optical morphologies on longitudinal section of bulk samples in Ti−Al−V−Nb alloys: 0Nb; (b) 2Nb; (c) 3.5Nb; (d) 5Nb; (e) 7Nb (The red dashed upper and lower regions are the deposited layer and Ti substrate, respectively)

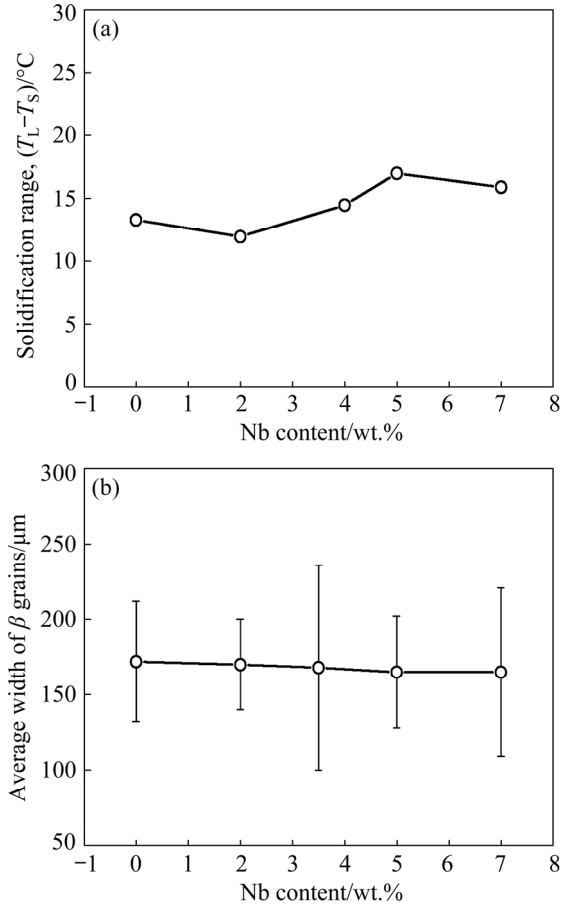

Fig. 8 Changes of calculated solidification range (T_L-T_S) using JMatPro software (a) and measured average width of columnar β grains (b) with Nb content in Ti−Al−V−Nb alloys

where coarse α grains result in the formation of these layer bands [31,32].

Figure 9 shows the microstructures near the substrate and surface on the longitudinal section of the bulk samples. The microstructure consisted of a fine basket-weave structure owing to the high cooling rate. During the deposition of Layer 1, its temperature decreased sharply from above T_L to T_β (T_β is the β transition temperature) and finally to a relatively low value. Then, a basket-weave microstructure was formed. Similarly, when Layers 2 and 3 were deposited, the whole region of Layer 1 was reheated to above T_β, resulting in a transformation from the basket-weave microstructure to the single β phase. Upon the subsequent rapid cooling process, a basket-weave microstructure formed in Layers 1, 2, and 3. When Layers 4 and 5 were deposited, a basket-weave microstructure was formed again due to the rapid cooling rate [33].

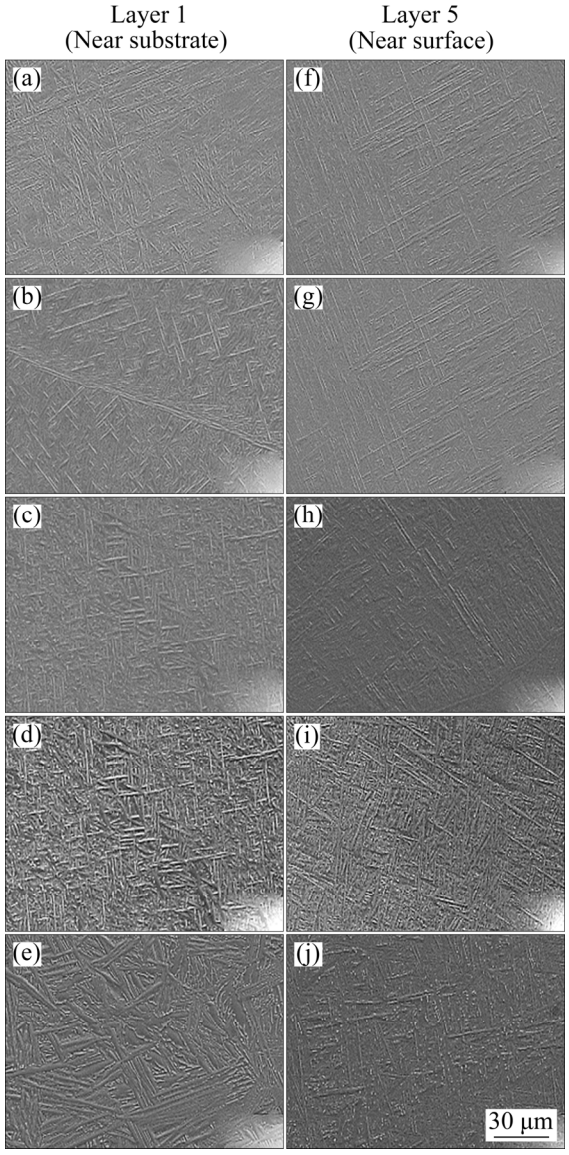

Fig. 9 Microstructures in Layer 1 (near substrate) (a−e) and Layer 5 (near surface) (f−j) on longitudinal section of bulk samples in Ti−Al−V−Nb alloys: (a, f) 0Nb; (b, g) 2Nb; (c, h) 3.5Nb; (d, i) 5Nb; (e, j) 7Nb

Figures 10(a−e) show the corresponding distributions of the α phase lath width in Layers 1 and 5 on longitudinal section of bulk samples. The distribution zone of the α phase size indicates uniformity. With increasing Nb content, the distribution zone of the α phase width became wider, and its uniformity deteriorated. In Layer 5, the distribution zones of the α phase width were narrow, e.g., 0.1−1.0 μm for 0Nb alloy and 0.1−1.5 μm for 7Nb alloy. Compared to Layer 5, the distribution of the α phase width was more diffused in Layer 1, e.g., 0.1−1.0 μm for 0Nb alloy and 0.1−3.5 μm for 7Nb alloy. Figure 10(f) shows the average α phase

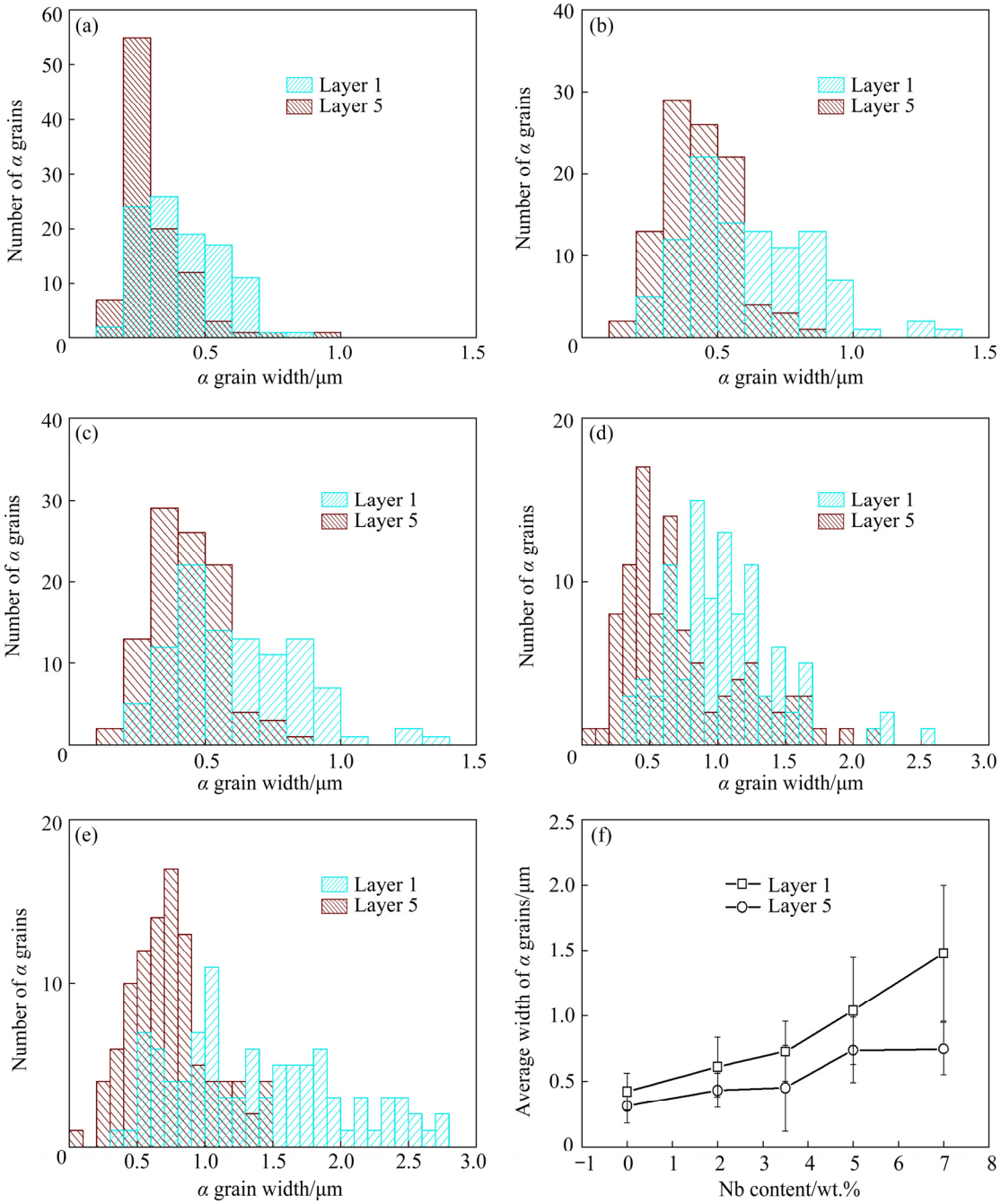

Fig. 10 Distributions of α phase lath width in Layers 1 and 5 on longitudinal section of bulk samples from blue and red statistics histograms, respectively: (a) 0Nb; (b) 2Nb; (c) 3.5Nb; (d) 5Nb; (e) 7Nb; (f) Changes in average width of α phase lath in Layers 1 and 5 with Nb content

width in Layers 1 and 5. The average width value of Layer 1 increased from 0.42 to 1.48 μm with increasing Nb content from 0 to 7 wt.%, and that of Layer 5 increased from 0.31 to 0.75 μm. Thus, the α phase formed near the Ti substrate was coarser than that near the surface. This result was attributed to different thermal histories. When Layers 2−5 of the powder were deposited, Layer 1 was reheated, forming a coarser α phase.

3.3 Mechanical properties of bulk samples

Figure 11(a) shows the XRD patterns of the cross-section near the surface of the bulk samples in Ti−Al−V−Nb alloys. The alloys showed similar peaks in the 2θ range of 30°−75°, which are characteristic of the α phase, whereas no peaks for the β phase were observed. The peak intensity of the α phase increased with increasing Nb content, suggesting that the volume fraction of the α phase

increased. In addition, the corresponding lattice parameters of the α phase (a and c) were calculated, as shown in Fig. 11(b). When the Nb content increased from 0 to 7 wt.%, a remained relatively constant at approximately 0.2934 nm. In contrast, c increased from 0.4673 to 0.4680 nm, and c/a ratio increased from 1.593 to 1.595. The solid solubility of Nb in the α phase was higher than that of V, resulting in a larger c and a larger c/a ratio, further increasing the hardness of the α phase.

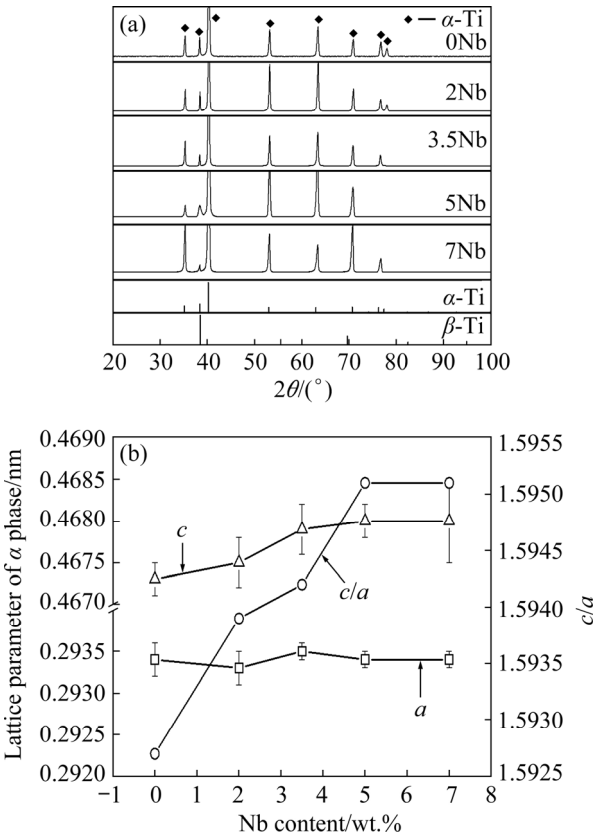

Fig. 11 XRD patterns on cross-section near surface of bulk samples in Ti−Al−V−Nb alloys (a) and changes in α phase lattice parameters, including c, a, and c/a ratio, with Nb content (b)

Figure 12(a) shows average Vickers hardness on the cross-section near the surface of the bulk samples. The average hardness increased from HV 430 to HV 466 with increasing Nb content from 0 to 3.5 wt.%, and then decreased from HV 466 to HV 423 with increasing Nb content up to 7 wt.%. The result has two explanations. Firstly, the volume fraction of the α phase increased with increasing Nb content, and the α phase becomes harder, thereby increasing the overall hardness. Secondly, the α phase width near the surface increased with increasing Nb content (Fig. 10), i.e., a coarsening α

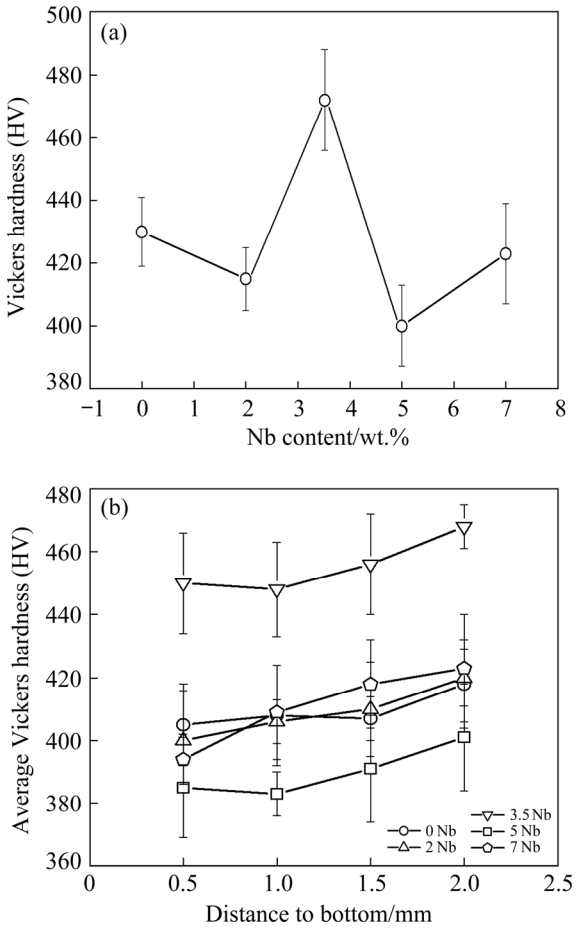

Fig. 12 Changes in average Vickers hardness on cross-section near surface (a) and on longitudinal section (b)

phase, which reduced the hardness. The 3.5Nb alloy exhibited the highest hardness among the five alloys when the matching relationship was improved. The average hardness decreased with increasing Nb content from 0 to 5 wt.%, suggesting that the negative effect of the α phase size was great. In contrast, it increased with increasing Nb content from 5 to 7 wt.% because of the positive effects of the α phase content. Figure 12(b) presents the Vickers hardness on the longitudinal sections of the bulk samples. The Vickers hardness increased slightly along the deposition direction from the substrate to the surface of all alloys. The changes in hardness in different cladding layers were related mainly to the α phase size. The α phase size near the surface was finer than that near the bottom, considering the effect of cycle heat treatment on the microstructure, as shown in Fig. 10, leading to higher hardness. Similarly, the 3.5Nb alloy exhibited the highest hardness among the five alloys regardless of the positions because of the

concurrent effects of the α phase size and its content.

4 Conclusions

(1) For the Ti−5.96Al−1.94V−3.54Nb alloy, the molten pool height was consistent with the spread layer thickness of the powder, which led to improved geometrical accuracy.

(2) The microstructure of the bulk samples contained similar columnar β phase grains, regardless of the Nb content. The basket-weave microstructure in the columnar grains was composed of α phase laths. The α phase size and its uniformity increased with increasing Nb content.

(3) The 3.5Nb alloy exhibited the highest Vickers hardness because of the optimal matching relationship between the α phase size and its content.

Acknowledgments

The authors are grateful for the financial support from the National Key Research and Development Program of China (No. 2016YFB1100103)

References

[1] JU J, LI J J, JIANG M, LI M Y, YANG L X, WANG K M, YANG C, KANG M D, WANG J. Microstructure and electrochemical corrosion behavior of selective laser melted Ti−6Al−4V alloy in simulated artificial saliva [J]. Transactions of Nonferrous Metals Society of China, 2021, 31: 167−177.

[2] DEBROY T, WEI H L, ZUBACK J S, MUKHERJEE T, ELMER J W, MILEWSKI J O, BEESE A M, WILSON-HEID A, DE A, ZHANG W. Additive manufacturing of metallic components—Process, structure and properties [J]. Progress in Materials Science, 2018, 92: 112−224.

[3] YANG X, WANG W L, MA W J, WANG Y, YANG J G, LIU S F, TANG H P. Corrosion and wear properties of micro-arc oxidation treated Ti6Al4V alloy prepared by selective electron beam melting [J]. Transactions of Nonferrous Metals Society of China, 2020, 30: 2132−2142.

[4] KHORASANI A, GIBSON I, AWAN U S, GHADERI A. The effect of SLM process parameters on density, hardness, tensile strength and surface quality of Ti−6Al−4V [J]. Additive Manufacturing, 2019, 25: 176−186.

[5] ZHANG X Y, FANG G, SANDER L, AMARANTE J B, AMIR A Z, ZHOU J. Effect of subtransus heat treatment on the microstructure and mechanical properties of additively manufactured Ti−6Al−4V alloy [J]. Journal of Alloys and Compounds, 2018, 735: 1562−1575.

[6] GUO K K, LIU C S, CHEN S Y, DONG H H, WANG S Y. High pressure EIGA preparation and 3D printing capability of Ti−6Al−4V powder [J]. Transactions of Nonferrous Metals Society of China, 2020, 30: 147−159.

[7] ZHU Y Y, CHEN B, TANG H B, CHENG X, WANG H M, LI J. Influence of heat treatments on microstructure and mechanical properties of laser additive manufacturing Ti−5Al−2Sn−2Zr−4Mo−4Cr titanium alloy [J]. Transactions of Nonferrous Metals Society of China, 2018, 28: 36−46.

[8] GALARRAGA H, WARREN R J, LADOS D A, DEHOFF R R, KIRKA M M, NANDWANA P, Effects of heat treatments on microstructure and properties of Ti−6Al−4V ELI alloy fabricated by electron beam melting (EBM) [J]. Materials Science and Engineering A, 2017, 685: 417−428.

[9] ZHU Z H, NIE K B, MUNROE P, DENG K K, GUO Y C, HAN J G. Synergistic effects of hybrid (SiC+TiC) nanoparticles and dynamic precipitates in the design of a high-strength magnesium matrix nanocomposite [J]. Materials Chemistry and Physics, 2021, 259: 124048.

[10] VILARO T, COLIN C, BARTOUT J D. As-fabricated and heat-treated microstructures of the Ti−6Al−4V alloy processed by selective laser melting [J]. Metallurgical and Materials Transactions A, 2011, 42: 3190−3199.

[11] LI P H, GUO W G, HUANG W D, SU Y, LIN X, YUAN K B. Thermomechanical response of 3D laser-deposited Ti−6Al−4V alloy over a wide range of strain rates and temperatures [J]. Materials Science and Engineering A, 2015, 647: 34−42.

[12] VRANCKEN B, THIJS L, KRUTH J P, HUMBEEK J V. Heat treatment of Ti6Al4V produced by selective laser melting: Microstructure and mechanical properties [J]. Journal of Alloys and Compounds, 2012, 541: 177−185.

[13] REN Y M, LIN X, FU X, TAN H, CHEN J, HUANG W D. Microstructure and deformation behavior of Ti−6Al−4V alloy by high-power laser solid forming [J]. Acta Materialia, 2017, 132: 82−95.

[14] ZHAO Z, CHEN J, TAN H, ZHANG G H, LIN X, HUANG W D. Achieving superior ductility for laser solid formed extra low interstitial Ti−6Al−4V titanium alloy through equiaxial alpha microstructure [J]. Scripta Materialia, 2018, 146: 187−191.

[15] SABBAN R, BAHL S, CHATTERJEE K, SUWAS S. Globularization using heat treatment in additively manufactured Ti−6Al−4V for high strength and toughness [J]. Acta Materialia, 2019, 162: 239−254.

[16] SUI Q X, MENG L T, WANG S H, LI P Z, YIN X T, WANG L. Effect of Nb addition on mechanical properties and corrosion behavior of Ti6Al4V alloy produced by selective laser melting [J]. Journal of Materials Research, 2020, 35: 571−579.

[17] KHAN M A, WILLIAMS R L, WILLIAMS D F. The corrosion behaviour of Ti−6Al−4V, Ti−6Al−7Nb and Ti−13Nb−13Zr in protein solutions [J]. Biomaterials, 1999, 20: 637.

[18] NIE K B, ZHU Z H, MUNROE P, DENG K K, HAN J G. Microstructure, tensile properties and work hardening behavior of an extruded Mg−Zn−Ca−Mn magnesium alloy [J]. Acta Metallurgica Sinica (English Letters), 2020, 33: 922−936.

[19] DONG C, DONG D D, WANG Q. Review of structural models for the compositional interpretation of metallic glasses [J]. International Materials Reviews, 2020, 65: 286−296.
[20] DONG C, WANG Q, QIANG J B, WANG Y M, JIANG N, HAN G, LI Y H, WU J, XIA J H. From clusters to phase diagrams: Composition rules of quasicrystals and bulk metallic glasses [J]. Journal of Physics D: Applied Physics, 2007, 40: R273−R291.
[21] DONG D D, ZHANG S, WANG Z R, DONG C. Nearest-neighbor coordination polyhedral clusters in metallic phases defined using Friedel oscillation and atomic dense packing [J]. Journal of Applied Crystallography, 2015, 48: 2002−2005.
[22] DONG D D, ZHANG S, WANG Z J, DONG C, HAUSSLER P. Composition interpretation of binary bulk metallic glasses via principal cluster definition [J]. Materials & Design, 2016, 96: 115−121.
[23] QIAN S N, DONG C, LIU T Y, QIN Q, WANG Q, WU Y W, GU L D, ZOU J X, HENG X W, PENG L M, ZENG X Q. Solute-homogenization model and its experimental verification in Mg−Gd-based alloys [J]. Journal of Materials Science & Technology, 2018, 34: 1132−1141.
[24] JIANG B B, WANG Q, WEN D H, XU F, CHEN G D, DONG C, SUN L X, LIAW T K. Effects of Nb and Zr on structural stabilities of Ti−Mo−Sn-based alloys with low modulus [J]. Materials Science and Engineering A, 2017, 687: 1−7.
[25] WANG Z R, QIANG J B, WANG Y M, WANG Q, DONG D D, DONG C. Composition design procedures of Ti-based bulk metallic glasses using the cluster-plus-glue-atom model [J]. Acta Materialia, 2016, 111: 366−376.
[26] KRUTH J P, FROVEN L, van VAERENBERJH J, MERCELIS P, ROMBOUTS M, LAUWERS B. Selective laser melting of iron-based powder [J]. Journal of Materials Processing Technology, 2004, 149: 616−622.
[27] NIU H J, CHANG I T H. Instability of scan tracks of selective laser sintering of high speed steel powder [J]. Scripta Materialia, 1999, 41: 1229−1234.
[28] LAN L, JIN X Y, GAO S, HE B, RONG Y H. Microstructural evolution and stress state related to mechanical properties of electron beam melted Ti−6Al−4V alloy modified by laser shock peening [J]. Journal of Materials Science & Technology, 2020, 50: 153−164.
[29] YANG J J, HAN J, YU H C, YIN J, GAO M, WANG Z M, ZENG X Y. Role of molten pool mode on formability, microstructure and mechanical properties of selective laser melted Ti−6Al−4V alloy [J]. Materials & Design, 2016, 110: 558−570.
[30] VRANCKEN B, THIJS L, KRUTH J P, HUMBEECK J V. Microstructure and mechanical properties of a novel β titanium metallic composite by selective laser melting [J]. Acta Materialia, 2014, 68: 150−158.
[31] NIE K B, ZHU Z H, DENG K K, HAN J G. Effect of extrusion temperature on microstructure and mechanical properties of a low-alloying and ultra-high strength Mg−Zn−Ca−Mn matrix composite containing trace TiC nanoparticles [J]. Journal of Magnesium and Alloys, 2020, 8: 676−691.
[32] WU X H, LIANG J, MEI J F, MITCHELL C, GOODWIN P S, VOICE W. Microstructures of laser-deposited Ti−6Al−4V [J]. Materials & Design, 2004, 25: 137−144.
[33] ZHU Y Y, TIAN X J, LI J, WANG H M. Microstructure evolution and layer bands of laser melting deposition Ti−6.5Al−3.5Mo−1.5Zr−0.3Si titanium alloy [J]. Journal of Alloys and Compounds, 2014, 616: 468−474.

基于团簇成分式设计激光增材制造 Ti−Al−V−Nb 系合金的显微组织与力学性能

刘田雨[1,2]，闵小华[1]，张 爽[3]，王存山[2]，董 闯[2,3]

1. 大连理工大学 材料科学与工程学院，大连 116024；2. 大连理工大学 三束材料改性教育部重点实验室，大连 116024；
3. 大连交通大学 材料科学与工程学院，大连 116028

摘 要：基于 Ti−6Al−4V 合金团簇成分式，用 Nb 替代团簇式中的 V 设计 Ti−Al−V−Nb 系合金，其团簇成分式为 $12[Al-Ti_{12}](AlTi_2)+5[Al-Ti_{14}](V,Nb)_2Ti$。采用激光增材制造技术制备不同 Nb 含量(0~6.96% Nb，质量分数)合金的单道熔覆层和块状试样，并对其成形性、显微组织和力学性能进行研究。结果表明，Nb 可以增加单道熔覆层的表面粗糙度，降低熔池高度，从而改善合金的铺展性。Ti−5.96Al−1.94V−3.54Nb (质量分数，%)合金由于熔池高度与预设沉积层厚度一致，表现出优异的几何精度。Ti−Al−V−Nb 系合金块体样品的组织由沿沉积方向外延生长的 β 柱状晶构成，而 β 柱状晶内为 α 板条构成的网篮组织。随着 Nb 含量的增加，α 板条的宽度增加，而其尺寸均匀性降低。合金的维氏硬度沿沉积方向度逐渐增加。由于 α 板条宽度和含量具有较好的匹配关系，所以 Ti−5.96Al−1.94V−3.54Nb 合金具有最高的维氏硬度。

关键词：Ti−Al−V−Nb 系合金；成分设计；激光增材制造；显微组织；力学性能

(Edited by Wei-ping CHEN)